Three-flat tests including mounting-induced deformations

Ulf Griesmann
Quandou Wang
Johannes Soons
National Institute of Standards and Technology
Manufacturing Engineering Laboratory
100 Bureau Drive
Gaithersburg, Maryland 20899-8223
E-mail: ulf.griesmann@nist.gov

Abstract. We investigate three-flat calibration methods based on rotational symmetry and mirror symmetry for absolute interferometric flatness measurements of circular flats in the presence of deformations caused by the support mechanism for the flats, which are a significant problem for large, heavy flats. We show that the mirror-symmetric component of the mounting-induced deformation can be determined by comparing flat test solutions based on mirror symmetry and on rotational symmetry, when the flats have identical deformations. We also describe a novel solution to the three-flat problem for three flats with identical mounting-induced deformations. In the new three-flat solution, the flat deformation is calculated along with the wavefront flatness errors for the three flats. Formulas for the uncertainty of three-flat test solutions are derived.
 [DOI: 10.1117/1.2784531]

Subject terms: interferometry; three-flat test; absolute flatness measurement; mounting-induced deformations; uncertainty.

Paper 060966R received Dec. 21, 2006; revised manuscript received Mar. 10, 2007; accepted for publication Mar. 16, 2007; published online Sep. 21, 2007.

1 Introduction

Interferometric figure metrology is a form of length metrology in which the distance, or more often distance variation, between a surface under test and a reference surface is measured at many locations on the surfaces simultaneously. Coherent light with a known wavelength serves as the length scale for the distance measurements. Phase-measuring two-beam interferometers have become widely used workhorses for form measurements of precision surfaces with low uncertainty. With increasing spread of interferometric metrology and increasing demand for low measurement uncertainties, interferometer calibration, which requires the separation of the form errors of the reference and test surfaces, has become a central problem of interferometric figure metrology. Efficient and well-understood methods for interferometer calibration are important to realize the potential of interferometry for measurements with uncertainties at and below the nanometer level. The past three decades have seen a gradual development of new methods, called *absolute* tests, for interferometer calibration, which parallels the development and adoption of interferometry. For the calibration of interferometers for measuring flatness errors, absolute tests known as full-aperture three-flat tests have largely superseded earlier calibration methods such as liquid-mirror flatness standards.[1–3]

A schematic overview of a Fizeau interferometer, and the arrangement of the reference surface $S_R(x,y)$ and the test surface $S_T(x,y)$, are shown in Fig. 1. A collimated beam, possibly containing some aberrations caused by the illumination optics, is sent to a transmission flat with reference surface S_R, where a fraction of the beam is reflected, while the remainder travels through the flat to the test surface. The reflected wave carries information about the flatness error of the reference surface to the detector. The transmitted fraction of the beam, which carries the same information as the reference beam, is partially reflected back by the test surface S_T, where it picks up information about the flatness error of the test surface. When the returning wave passes through the reference surface, the original contribution of the reference surface to the flatness error of the wavefront is subtracted, if the interferometer is correctly aligned to minimize the number of fringes. The reflected waves travel superimposed to the detector, where the surfaces are imaged and the combined flatness error of test and reference wavefronts is measured. In the coordinate system of the interferometer, the combined wavefront $W(x,y)$ is

$$W(x,y) = W_R(-x,y) + W_T(x,y), \tag{1}$$

where $W_R(-x,y)$ stands for the wavefront reflected by the reference flat, and $W_T(x,y)$ for the wavefront reflected by the test surface. We assume that reference and test flats are circular with diameter d and therefore $x^2+y^2 \leq d^2/4$. The origin of the coordinate system is at the center of the flats. [It must be borne in mind that Eq. (1) describes an idealized interferometer. In many real interferometers, stray wavefronts from surfaces other than reference and test surfaces reach the detector and affect the measurements. The consequences—for example, hot spots and ghost fringes—will increase the measurement uncertainty.] In a Fizeau interferometer, the flatness error of the surface, $S(x,y)$, is half of the wavefront error $W(x,y)$:

$$S(x,y) = \frac{1}{2} W(x,y). \tag{2}$$

0091-3286/2007/$25.00 © 2007 SPIE

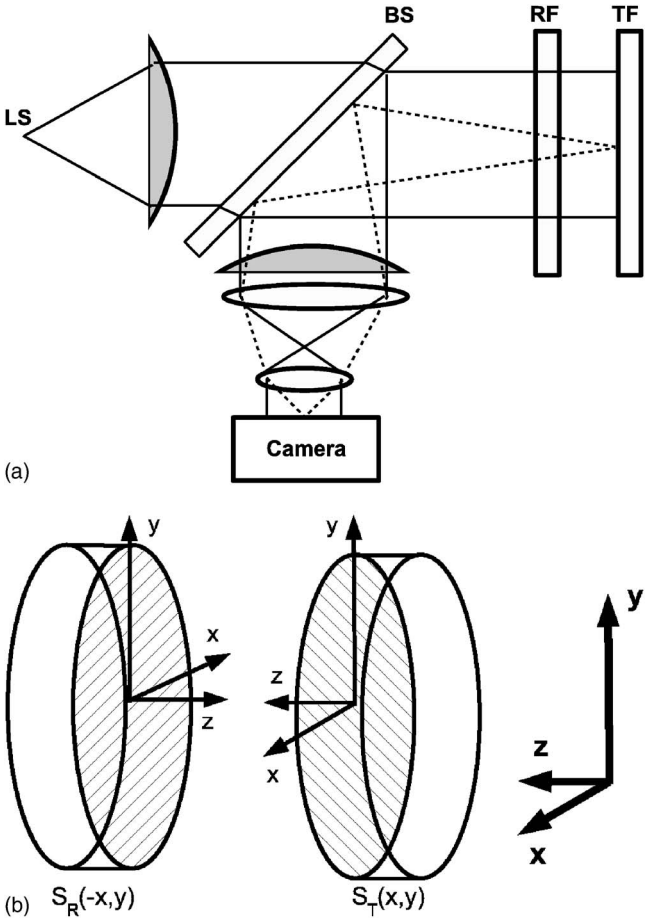

Fig. 1 (a) Schematic overview of a Fizeau interferometer. Light emitted by a light source (LS) is collimated and illuminates a reference flat (RF) and a test flat (TF). A beamsplitter (BS) directs a fraction of the return beams to the imaging arm of the interferometer. The illumination optical path is indicated with continuous lines; dashed lines indicate the imaging optical path. (b) The coordinate systems we use for the reference surface S_R and the test surface S_T. The coordinate system of the interferometer is indicated with bold arrows.

The interferometer compares flats in pairs, and the purpose of a flat test is a determination of the flatness error of each flat from pairwise comparisons of at least three flats. For example, three flats A, B, and C can be compared using the measurement sequence (BA, CA, CB). In this paper we use the convention that the first letter in a pair such as BA refers to the reference flat, the second to the test flat. The results of the three measurements, which have the same form as Eq. (1), can be written in a matrix equation as follows:

$$\begin{pmatrix} W_1(x,y) \\ W_2(x,y) \\ W_3(x,y) \end{pmatrix} = \begin{pmatrix} 1 & 0 & 1 & 0 \\ 1 & 0 & 0 & 1 \\ 0 & 1 & 0 & 1 \end{pmatrix} \begin{pmatrix} W_A(x,y) \\ W_B(x,y) \\ W_B(-x,y) \\ W_C(-x,y) \end{pmatrix}. \tag{3}$$

In this equation, W_A, W_B, and W_C are the wavefronts reflected by the three flats, and W_1, W_2, and W_3 are the measurements of the combined wavefront errors.

In this paper, we concentrate on the effect of deformations caused by the mechanical support for vertically mounted flats on the solutions of the three-flat problem. For small flats, mounting-induced deformations may be negligible, but the form error of large, heavy flats will usually be affected by the support mechanism for the flats. Section 2 is a concise overview of methods for solving the three-flat problem. This is followed by a discussion of the effect of mounting-induced deformations on the flat test solutions. Section 4 contains numerical simulations of three-flat tests to illustrate their performance in the presence of mounting-induced deformations of the flats. We then discuss, in Sec. 5, a practical implementation of three-flat tests for the calibration of 325-mm reference flats for use with XCALIBIR ("Extremely Accurate Calibration Interferometer") at the National Institute of Standards and Technology (NIST). Finally, in Sec. 6, we discuss the measurement uncertainty of three-flat tests and derive formulas for the calculation of the uncertainty of three-flat test solutions.

2 A Summary of Three-Flat Tests

We now show how to solve the three-flat equation (3), in a way that emphasizes the general structure of the solutions. In subsequent sections, we then describe specific solutions based on two different symmetries. The three-flat equation (3) can only be solved for points on the y axis,[4] because, in general, $W(x,y) \neq W(-x,y)$ and the matrix in Eq. (3) is rank-deficient. However, a partial solution for Eq. (3) can be found by splitting every wavefront $W(x,y)$ in Eq. (3) into a component $I(x,y)$ that is *invariant* under reflections at the y axis $[I(x,y)=I(-x,y)$ for all $y]$ and a residuum $V(x,y)$:

$$W(x,y) = I(x,y) + V(x,y). \tag{4}$$

We call $V(x,y)$ the *variant* component of $W(x,y)$. When the wavefronts in Eq. (3) are split according to Eq. (4), two equations for $I(x,y)$ and $V(x,y)$ result. If solutions for $I(x,y)$ and $V(x,y)$ can be found, the sum of those solutions is a solution of Eq. (3). For the component $I(x,y)$, the number of unknowns in Eq. (3) is reduced by one:

$$\begin{pmatrix} I_1(x,y) \\ I_3(x,y) \\ I_4(x,y) \end{pmatrix} = \begin{pmatrix} 1 & 1 & 0 \\ 1 & 0 & 1 \\ 0 & 1 & 1 \end{pmatrix} \begin{pmatrix} I_A(x,y) \\ I_B(x,y) \\ I_C(x,y) \end{pmatrix}. \tag{5}$$

Unlike in Eq. (3), the measurements are now numbered as in Fig. 2 to make room for an additional measurement, which are needed below. The coefficient matrix of Eq. (5) has an inverse, and the invariant components I_A, I_B, and I_C of the three-flat test solutions can be expressed in terms of the invariant components I_1, I_3 and I_4 of the measurements:

$$\begin{pmatrix} I_A(x,y) \\ I_B(x,y) \\ I_C(x,y) \end{pmatrix} = \frac{1}{2} \begin{pmatrix} 1 & 1 & -1 \\ 1 & -1 & 1 \\ -1 & 1 & 1 \end{pmatrix} \begin{pmatrix} I_1(x,y) \\ I_3(x,y) \\ I_4(x,y) \end{pmatrix}. \tag{6}$$

For the variant wavefront components $V(x,y)$, the equation

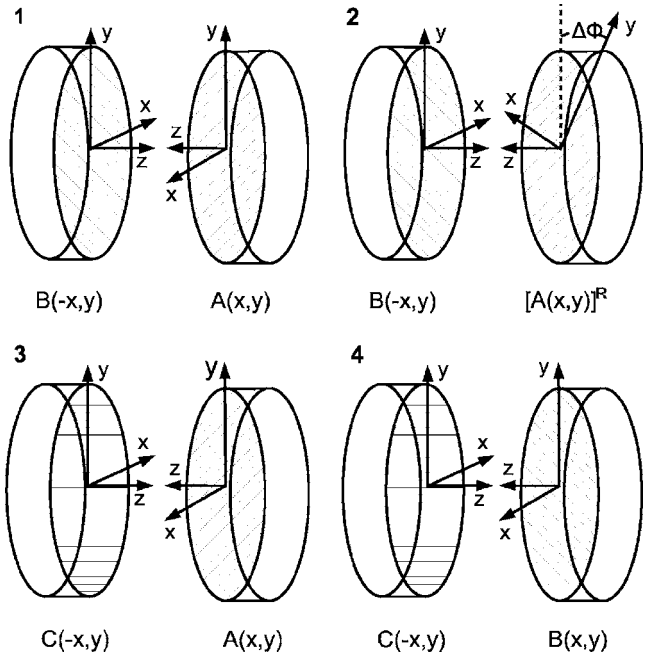

Fig. 2 Measurement sequence (*BA*, *BA*^{R}, *CA*, *CB*) for the comparison of three flats *A*, *B*, and *C*. In the second measurement the *azimuthal average*, or *rotation average*, of flat *A* is measured against reference flat *B* (see Section 2.3).

$$\begin{pmatrix} V_1(x,y) \\ V_3(x,y) \\ V_4(x,y) \end{pmatrix} = \begin{pmatrix} 1 & 0 & 1 & 0 \\ 1 & 0 & 0 & 1 \\ 0 & 1 & 0 & 1 \end{pmatrix} \begin{pmatrix} V_A(x,y) \\ V_B(x,y) \\ V_B(-x,y) \\ V_C(-x,y) \end{pmatrix}, \tag{7}$$

must be solved, which has the same number of variables as Eq. (3). A solution for this equation can only be found when one of the unknown variables is determined with an additional measurement. Since it does not matter which of the variables on the right side of Eq. (7) is determined, we assume that, in some way, a measurement of the variant wavefront component $V_B(-x,y)$ of reference flat *B*, is made:

$$V_2(x,y) = V_B(-x,y). \tag{8}$$

This measurement is included with the measurements in Eq. (7):

$$\begin{pmatrix} V_1(x,y) \\ V_2(x,y) \\ V_3(x,y) \\ V_4(x,y) \end{pmatrix} = \begin{pmatrix} 1 & 0 & 1 & 0 \\ 0 & 0 & 1 & 0 \\ 1 & 0 & 0 & 1 \\ 0 & 1 & 0 & 1 \end{pmatrix} \begin{pmatrix} V_A(x,y) \\ V_B(x,y) \\ V_B(-x,y) \\ V_C(-x,y) \end{pmatrix}. \tag{9}$$

The inverse of the matrix in Eq. (9) exists, and the equation can be solved for the variant wavefront components of the flats:

$$\begin{pmatrix} V_A(x,y) \\ V_B(x,y) \\ V_B(-x,y) \\ V_C(-x,y) \end{pmatrix} = \begin{pmatrix} 1 & -1 & 0 & 0 \\ 1 & -1 & -1 & 1 \\ 0 & 1 & 0 & 0 \\ -1 & 1 & 1 & 0 \end{pmatrix} \begin{pmatrix} V_1(x,y) \\ V_2(x,y) \\ V_3(x,y) \\ V_4(x,y) \end{pmatrix}. \tag{10}$$

This equation contains two solutions for the variant component V_B. One of the solutions is simply the measurement in Eq. (8). When this solution and the solution for V_C are reflected at the *y* axis, one obtains

$$\begin{aligned} V_B(x,y) &= V_2(-x,y), \\ V_C(x,y) &= -V_1(-x,y) + V_2(-x,y) + V_3(-x,y). \end{aligned} \tag{11}$$

These equations can then be combined with the solution for V_A into one matrix equation:

$$\begin{pmatrix} V_A(x,y) \\ V_B(x,y) \\ V_C(x,y) \end{pmatrix} = \begin{pmatrix} 1 & -1 & 0 & 0 & 0 \\ 0 & 0 & 0 & 1 & 0 \\ 0 & 0 & -1 & 1 & 1 \end{pmatrix} \begin{pmatrix} V_1(x,y) \\ V_2(x,y) \\ V_1(-x,y) \\ V_2(-x,y) \\ V_3(-x,y) \end{pmatrix}. \tag{12}$$

Finally, the solutions for the invariant and variant components can be added [Eq. (4)], which results in a general solution for the wavefront flatness errors of all three flats in terms of reflection invariant $I_k(x,y)$ and variant residuals $V_k(x,y)$ of the measured wavefronts:

$$\begin{pmatrix} W_A(x,y) \\ W_B(x,y) \\ W_C(x,y) \end{pmatrix} = \frac{1}{2} \begin{pmatrix} 1 & 1 & -1 & 2 & -2 & 0 & 0 & 0 \\ 1 & -1 & 1 & 0 & 0 & 0 & 2 & 0 \\ -1 & 1 & 1 & 0 & 0 & -2 & 2 & 2 \end{pmatrix} \times \begin{pmatrix} I_1(x,y) \\ I_3(x,y) \\ I_4(x,y) \\ V_1(x,y) \\ V_2(x,y) \\ V_1(-x,y) \\ V_2(-x,y) \\ V_3(-x,y) \end{pmatrix}. \tag{13}$$

In the following two sections, decompositions of wavefronts as in Eq. (4) based on mirror symmetry and rotation symmetry are discussed and the resulting solutions of the three-flat test are summarized.

2.1 *Test Solutions Based on Mirror Symmetry*

The condition $W(-x,y)=W(x,y)$ characterizes functions that are symmetric under reflection in the *y* axis. We define a reflection operator $[\cdot]^x$, which mirrors a wavefront $W(x,y)$ in the *y* axis:

$$W^x(x,y) \overset{\text{def}}{=} [W(x,y)]^x \overset{\text{def}}{=} W(-x,y). \tag{14}$$

For any given wavefront $W(x,y)$, the reflection operator can be used to construct a wavefront that is invariant under reflection in the y axis:

$$W^e \overset{\text{def}}{=} \frac{1}{2}(W + W^x). \tag{15}$$

From here on we omit function arguments when the meaning of an equation is clear without them. We call W^e the *x-even* component of wavefront W, which can now be written as

$$W = W^e + W^o, \tag{16}$$

where W^o is the difference between W and W^e, which we call the *x-odd* component of W. It follows that

$$W^o \overset{\text{def}}{=} W - W^e = \frac{1}{2}(W - W^x), \tag{17}$$

and from Eq. (17) it follows that the x-odd wavefront component W^o is antisymmetric:

$$[W^o]^x = -W^o. \tag{18}$$

It is also possible to devise flat tests based on mirror symmetry using decompositions of wavefronts into components with two symmetry lines.[5,6] In this paper, we limit the discussion of solutions based on mirror symmetry to the reflection in the y axis only.

The general form of the flat test solutions is the same as Eq. (13). When the measured wavefronts $W_1, \ldots, W_4$ are written as sums of x-even and x-odd components, a single equation for the wavefront flatness errors for all flats in terms of x-even and x-odd functions results:

$$\begin{pmatrix} W_A(x,y) \\ W_B(x,y) \\ W_C(x,y) \end{pmatrix} = \frac{1}{2}\begin{pmatrix} 1 & 1 & -1 & 2 & -2 & 0 \\ 1 & -1 & 1 & 0 & -2 & 0 \\ -1 & 1 & 1 & 2 & -2 & -2 \end{pmatrix} \times \begin{pmatrix} W_1^e(x,y) \\ W_3^e(x,y) \\ W_4^e(x,y) \\ W_1^o(x,y) \\ W_2^o(x,y) \\ W_3^o(x,y) \end{pmatrix}. \tag{19}$$

In many cases, three-flat test solutions are not unique. For example, an alternative solution to Eq. (19) can be found easily. When the antisymmetry of the x-odd wavefronts is taken into account, the following equation for the x-odd wavefronts follows from Eq. (9):

$$\begin{pmatrix} W_1^o(x,y) \\ W_2^o(x,y) \\ W_3^o(x,y) \\ W_4^o(x,y) \end{pmatrix} = \underbrace{\begin{pmatrix} 1 & -1 & 0 \\ 0 & -1 & 0 \\ 1 & 0 & -1 \\ 0 & 1 & -1 \end{pmatrix}}_{=\mathbf{C}} \begin{pmatrix} W_A^o(x,y) \\ W_B^o(x,y) \\ W_C^o(x,y) \end{pmatrix}. \tag{20}$$

This system of equations is overdetermined, and the matrix $\mathbf{C}$ in Eq. (20) cannot be inverted. However, its pseudoinverse, $(\mathbf{C}^T\mathbf{C})^{-1}\mathbf{C}^T$, exists and can be used to obtain the least-squares solution for the x-odd wavefront components:

$$\begin{pmatrix} W_A^o(x,y) \\ W_B^o(x,y) \\ W_C^o(x,y) \end{pmatrix} = \frac{1}{3}\begin{pmatrix} 2 & -3 & 1 & -1 \\ 0 & -3 & 0 & 0 \\ 1 & -3 & -1 & -2 \end{pmatrix} \begin{pmatrix} W_1^o(x,y) \\ W_2^o(x,y) \\ W_3^o(x,y) \\ W_4^o(x,y) \end{pmatrix}. \tag{21}$$

This solution for the x-odd wavefront components can be added to the solution for the x-even components, Eq. (6), which results in the following three-flat test solution:

$$\begin{pmatrix} W_A(x,y) \\ W_B(x,y) \\ W_C(x,y) \end{pmatrix} = \frac{1}{6}\begin{pmatrix} 3 & 3 & -3 & 4 & -6 & 2 & -2 \\ 3 & -3 & 3 & 0 & -6 & 0 & 0 \\ -3 & 3 & 3 & 2 & -6 & -2 & -4 \end{pmatrix} \times \begin{pmatrix} W_1^e(x,y) \\ W_3^e(x,y) \\ W_4^e(x,y) \\ W_1^o(x,y) \\ W_2^o(x,y) \\ W_3^o(x,y) \\ W_4^o(x,y) \end{pmatrix}. \tag{22}$$

We return to Eq. (22) in the section on uncertainty (Sec. 6).

2.2 *A Test Solution Based on Continuous Rotation Symmetry*

A subspace of reflection-invariant functions consists of those invariant under continuous rotations. The use of rotation-invariant functions for solving the three-flat problem was first described by Küchel.[7] For every wavefront $W(r,\phi)$, in polar coordinates, a rotation-symmetric function can be derived by averaging $W(r,\phi)$ in the azimuthal direction. The *azimuthal average*, or *rotation average*, of $W(r,\phi)$ is defined as

$$W^R(r) \overset{\text{def}}{=} \frac{1}{2\pi}\int_0^{2\pi} W(r,\phi)\,\mathrm{d}\phi. \tag{23}$$

The integral on the right-hand side of Eq. (23) can be thought of as an operator $[\cdot]^R$,

$$[\cdot]^R \overset{\text{def}}{=} \frac{1}{2\pi}\int_0^{2\pi} \cdot\,\mathrm{d}\phi, \tag{24}$$

which we call the *azimuthal averaging operator*. Applying the azimuthal averaging operator to a wavefront $W(r,\phi)$

removes the rotationally varying component of the wavefront. Similar to Eq. (16), any wavefront W can thus be written as the sum of a rotation-invariant component and a component that changes under rotations:

$$W = W^R + \Omega, \tag{25}$$

where Ω is the difference of W and W^R. The definition of the azimuthal average implies that the rotationally variant wavefront component Ω has an azimuthal average of zero[8]:

$$[\Omega]^R = [W]^R - [W^R]^R = [W]^R - [W]^R = 0. \tag{26}$$

When the measured wavefronts $W_1, \ldots, W_4$ are broken up into rotation-nvariant and -variant components and are inserted into Eq. (13), it becomes an equation for the wavefront flatness errors for all three flats in terms of rotation-invariant and -variant components of the measurements:

$$\begin{pmatrix} W_A(x,y) \\ W_B(x,y) \\ W_C(x,y) \end{pmatrix} = \frac{1}{2}\begin{pmatrix} 1 & 1 & -1 & 2 & -2 & 0 & 0 & 0 \\ 1 & -1 & 1 & 0 & 0 & 0 & 2 & 0 \\ -1 & 1 & 1 & 0 & 0 & -2 & 2 & 2 \end{pmatrix} \times \begin{pmatrix} W_1^R(x,y) \\ W_3^R(x,y) \\ W_4^R(x,y) \\ \Omega_1(x,y) \\ \Omega_2(x,y) \\ \Omega_1(-x,y) \\ \Omega_2(-x,y) \\ \Omega_3(-x,y) \end{pmatrix}. \tag{27}$$

2.3 *How to Measure Ω_B and W_B^o*

In the derivation of the three-flat test solutions in Eqs. (27), (19), and (22) we assumed that the variant flatness error component of reference flat B in Eq. (7) is determined in a separate measurement. For the solution based on rotation symmetry [Eq. (27)], $\Omega_B(-x,y)$, or Ω_B^x, must be measured, and for the solution based on mirror symmetry it is the wavefront component $W_B^o(-x,y)$, or $(W_B^x)^o$, that must be measured. It is easily seen that the measurement

$$W_2 = W_B^x + W_A - \Omega_A = W_B^x + W_A^R, \tag{28}$$

in which the *azimuthal average* of flat A is measured against reference flat B, can be used to determine the variant wavefront components of reference flat B for *both* types of flat test. When the variant wavefront components for rotation symmetry and mirror symmetry are calculated from Eq. (28), it follows that

$$\Omega_2 = \Omega_B^x \tag{29}$$

and

$$W_2^o = [W_B^x]^o. \tag{30}$$

These are the wavefront components that are needed to solve Eq. (7) for the cases of rotational symmetry [Eq. (29)] and mirror symmetry [Eq. (30)].

There are two ways of realizing the measurement in Eq. (28). Either a measurement of Ω_A is made, which is then subtracted from the measurement W_1, or a procedure to directly measure reference flat B against the azimuthal average of flat A is used. In a seminal paper, Parks[9] describes the rotational shearing, or rotational differencing, method for calculating Ω_A. This is done by making two measurements of flat A against reference flat B, where flat A is rotated by an angle Φ in the second measurement. If W_α and W_β denote the two measurements and $[\cdot]^\Phi$ is an operator that rotates a wavefront by an angle Φ, then

$$\begin{aligned} W_\alpha &= W_B^x + W_A = W_B^x + W_A^R + \Omega_A, \\ W_\beta &= W_B^x + [W_A]^\Phi = W_B^x + W_A^R + [\Omega_A]^\Phi. \end{aligned} \tag{31}$$

Subtracting the first equation from the second, and defining $\Delta(r,\phi) \overset{\text{def}}{=} W_\beta(r,\phi) - W_\alpha(r,\phi)$, results in a difference equation for the rotationally variant component of the rotated flat,

$$[\Omega_A]^\Phi - \Omega_A = \Delta. \tag{32}$$

The difference equation can be written in polar coordinates as

$$\Omega_A(r,\phi-\Phi) - \Omega_A(r,\phi) = \Delta(r,\phi). \tag{33}$$

We now briefly outline the method of solving Eq. (33) to explain how the flat test solutions in the following sections were calculated. The reader is referred to the original literature for the details. The difference equation (33) can be solved by expanding Ω_A and Δ into series of complete, orthogonal functions on the unit disk and solving the resulting algebraic equation for the coefficients, or "frequencies", of the series. Well-known basis functions on the unit disk are Zernike functions,[10] harmonic functions,[11] or, when the unit disk is discretized in the radial direction into a set of concentric circles,[12,13] trigonometric functions. In the flat test solutions of Parks[9] and Fritz[14] Ω_A and Δ are expressed as Zernike series:

$$\begin{aligned} \Omega_A(\rho,\phi) &= \sum_{n=0}^{\infty}\sum_{l=-n}^{n} o_{nl} R_n^{|l|}(\rho) e^{il\phi}, \\ \Delta(\rho,\phi) &= \sum_{n=0}^{\infty}\sum_{l=-n}^{n} d_{nl} R_n^{|l|}(\rho) e^{il\phi}, \end{aligned} \tag{34}$$

where ρ is the dimensionless normalized radius ranging from 0 at the center to 1 at the edge of the flat. The functions $R_n^{|l|}(\rho)$ are polynomials in ρ. Equation (33) can be rewritten using Eq. (34) as

$$\sum_{n=0}^{\infty}\sum_{l=-n}^{n} [o_{nl}(e^{-il\Phi}-1) - d_{nl}] R_n^{|l|}(\rho) e^{il\phi} = 0. \tag{35}$$

For Eq. (35) to hold, the coefficients in the square brackets must be zero for all n and l, because the Zernike polynomials are orthogonal. The result is a relation that allows the

coefficients of Ω_A to be calculated from the coefficients of the measured quantity Δ:

$$o_{nl} = \frac{d_{nl}}{\exp(-il\Phi) - 1}. \tag{36}$$

Thus, the rotationally variant component Ω_A can be calculated from the difference $\Delta = W_\beta - W_\alpha$, as long as none of the denominators in Eq. (36) is zero. Using the relation $\exp(-i\pi) = -1$, it is easily seen that the denominator in Eq. (36) vanishes when $l\Phi$ is equal to a multiple of π. A rotation angle that is an integer fraction of the full circle would be a poor choice, because it would lead to a large number of singular terms in the series for Ω_A. Even with a better choice of Φ, Eq. (36) can be near-singular for some n, l, which amplifies the uncertainties in the coefficients d_{nl} for those terms. This, in turn, causes large uncertainties in the coefficients o_{nl}. The solution to this problem is to use more than one angle of rotation.[12,15] Any choice of rotation angle Φ must lead to the same set of coefficients o_{nl}. This suggests that the calculation of the coefficients o_{nl}can be improved by choosing *M incommensurate* rotation angles Φ_k instead of one rotation angle, and calculating the coefficients using a weighted average

$$o_{nl} = \sum_{k=1}^{M} w_k \frac{d_{k,nl}}{\exp(-il\Phi_k) - 1}, \tag{37}$$

where $d_{k,nl}$ are the coefficients of Δ for the rotation angle Φ_k. The normalized weights

$$w_k = \frac{|\exp(-il\Phi_k) - 1|^2}{\sum_{k=1}^{M} |\exp(-il\Phi_k) - 1|^2} \tag{38}$$

reduce the contributions from near-singular terms in Eq. (37), because those terms have the smallest weights. It has also been shown that the choice of weights in Eq. (38) is optimal for data affected by Gaussian noise with zero mean.[12]

For reasons of symmetry, harmonic functions on the unit disk[11] have the same angular dependence as Zernike functions. The functions Ω_A and Δ can be expanded into series of orthogonal harmonic functions:

$$\Omega_A(\rho, \phi) = \sum_{n=0}^{\infty} \sum_{l=-n}^{n} o_{nl} J_l(2\pi\rho\lambda_{nl}) e^{il\phi}, \tag{39}$$

where J_l is the l'th-order Bessel function of the first kind. The scaling factors λ_{nl}, which ensure that the harmonic functions are orthogonal on the unit disk, are the positive n'th roots of the derivatives $\mathrm{d}J_l(2\pi\rho)/\mathrm{d}\rho = 0$. Harmonic series can be used for solving Eq. (33) in the same way as Zernike series. Unlike Zernike polynomials of high orders, harmonic functions of high orders do not have large derivatives near the unit circle, which makes harmonic functions better suited than Zernike functions to describe a wavefront when a large number of terms are needed.

Finally, the circular area of the flats can be construed as a family of concentric, one-dimensional azimuthal profiles. The sets of azimuthal profiles for Ω_A and Δ, for a fixed radius r can be expanded into a Fourier series:

$$\Omega_A^r(\phi) = \sum_{l=-\infty}^{\infty} o_l e^{il\phi}, \tag{40}$$

which, again, has the same angular dependence as Zernike and harmonic functions. Equation (33) is solved for each concentric circle. This approach, used by Bourgeois et al.[13] and Freischlad,[12] is mathematically equivalent to the use of Zernike series, but has the great advantage of numerical economy, because there is currently no equivalent to the fast Fourier transform for Zernike series or harmonic series. The other—related—advantage of the Fourier series approach is that the Fourier transform of a sampled azimuthal profile contains all the information that is present in the profile. Zernike and harmonic series usally must be truncated before the coefficients contain all the information present in the data, or their calculation becomes too time-consuming.

The second approach to realizing the measurement W_2 in Eq. (28) is the *N*-position averaging method described by Evans and Kestner,[8,16,17] which directly approximates the measurement of reference flat *B* against the azimuthal average of flat *A*. In it, *N* measurements of flat *A* against reference flat *B* are averaged, and after each of the measurements, flat *A* is rotated by an angle $\Phi = 2\pi/N$:

$$W_2 = \frac{1}{N}\sum_{k=0}^{N-1} (W_B^x + [W_A]^{k\Phi}) = W_B^x + W_A^R + \underbrace{\frac{1}{N}\sum_{k=0}^{N-1} [\Omega_A]^{k\Phi}}_{\substack{N\to\infty \\ \to\ 0}}. \tag{41}$$

For realistic wavefronts, the average term on the right-hand side of Eq. (41) converges to zero with increasing *N*, in an approximation of Eq. (26).[8,16,18] When the *N*-position method is implemented, *N* must be chosen large enough to ensure that the flatness error of flat *A* contains only a negligible component with *N*-fold rotational symmetry and the azimuthal average is approximated within the intended uncertainty. The *N*-position averaging method thus requires *a priori* knowledge about the flatness errors of the parts under test, which is not required in the rotational differencing method.

Up to now, we have shown that the three-flat problem can be solved when a measurement is made in which at least one flat is rotated. From a mathematical point of view, a measurement involving a rotated flat [see Eq. (28)] is not the only one that can be made to solve the three-flat equations. Instead, reference flat *B* can be measured against the reflection-symmetric component of test flat *A* as follows:

$$W_2 = W_B^x + W_A - W_A^o = W_B^x + W_A^e. \tag{42}$$

When the *x*-odd component is calculated from Eq. (42), the result is

$$W_2^o = [W_B^x]^o. \tag{43}$$

The measurement of Eq. (42) can be used to find a solution for the three-flat problem based on mirror symmetry. It can be realized by averaging two measurements of reference flat *B* against flat *A* where in one of the measurements flat *A* is reflected *physically* in the *y* axis. Alternatively, the two measurements can be subtracted, which yields the *x*-odd

component of the flatness error of flat A. In practice, the reflection of a flat surface in the y axis is not possible, because optical flats are not idealized mathematical planes but thick plates of glass. When flat A is reflected in the y axis by rotating it about the y axis by an angle of π, the reflected surface must be measured through the bulk of flat A, which introduces an unknown measurement error. This is the reason for the central role of the azimuthal average in solving the three-flat problem.

3 Mounting-Induced Deformations

The form errors caused by the support mechanism of the flats are a long-standing problem in interferometric flatness metrology, especially for large, heavy flats. Deformations lead to a problem in the measurement W_2 of the measurement sequence in Fig. 2, because deformations due to the mechanical support of a flat will, in good approximation, remain stationary when the flat is rotated. This can lead to a significant error in the measurement W_2, which, in turn, affects the three-flat solutions for all flats. In this section we show that the mounting-induced deformation of the flats can be determined together with the flatness errors of the flats.

Some simplifying assumptions must be made to make the problem tractable. First, we assume that all flats are mounted in the same way, which leads to identical deformations $D(x,y)$, and we assume that the deformation is independent of the rotation angle of the flats. When the equations for the measurements in the sequence (BA, BA^R, CA, CB), shown in Fig. 2, are rewritten to include the deformation, D, the result is

$$\begin{aligned}
\tilde{W}_1(x,y) &= W_B^x + D^x + W_A + D = W_B^x + W_A + 2D^e,\\
\tilde{W}_2(x,y) &= W_B^x + D^x + W_A^R + D = W_B^x + W_A^R + 2D^e,\\
\tilde{W}_3(x,y) &= W_C^x + D^x + W_A + D = W_C^x + W_A + 2D^e,\\
\tilde{W}_4(x,y) &= W_C^x + D^x + W_B + D = W_C^x + W_B + 2D^e.
\end{aligned} \tag{44}$$

The tilde is used to distinguish wavefront measurements including a deformation term from the measurements in Eq. (3), in which the deformation was neglected. Equation (44) shows that only the x-even component of the deformation, D^e, remains in the measurements, because the x-odd components cancel out. This has an important practical consequence: when the mechanical support for the flats imparts a deformation with an x-odd component, this cannot be detected in a pairwise comparison of the flats. The flat mount must be designed to ensure that any deformation it imparts to the flats is purely x-even. An example is the mount shown in Fig. 8 (Sec. 5), which is symmetric with respect to a vertical line through the center of the flat. In the following we assume that $D(x,y)$ is an x-even function. In addition, we assume that the azimuthal average of $D(x,y)$ is zero: $[D]^R=0$, because a rotation-invariant deformation cannot be distinguished from the rotation-invariant flatness error component of the flats.

It is instructive to compare flat test solutions based on mirror symmetry and rotational symmetry when mounting-induced distortions of the flats are present. We first consider the effect of a deformation on the flat test solutions based on mirror symmetry. When measurements $\tilde{W}_1,\ldots,\tilde{W}_4$, which include the deformation, are used in Eq. (19) to calculate the solutions for the wavefront flatness errors of flats A, B, and C, the flat test solutions are

$$\begin{pmatrix} \tilde{W}_A(x,y)\\ \tilde{W}_B(x,y)\\ \tilde{W}_C(x,y)\end{pmatrix}_x = \begin{pmatrix} W_A(x,y)\\ W_B(x,y)\\ W_C(x,y)\end{pmatrix}_x + \begin{pmatrix} D(x,y)\\ D(x,y)\\ D(x,y)\end{pmatrix}. \tag{45}$$

The subscript x denotes solutions based on mirror symmetry. The same result is obtained for the solution Eq. (22). The deformation of the flats is contained in the solutions for the wavefront flatness error of the three flats. In the same way, using Eq. (27), solutions for the deformed flats based on rotational symmetry are derived:

$$\begin{aligned}
\begin{pmatrix} \tilde{W}_A(x,y)\\ \tilde{W}_B(x,y)\\ \tilde{W}_C(x,y)\end{pmatrix}_R &= \begin{pmatrix} W_A(x,y)\\ W_B(x,y)\\ W_C(x,y)\end{pmatrix}_R + \begin{pmatrix} 2 & -2 & 0 & 0 & 0\\ 0 & 0 & 0 & 2 & 0\\ 0 & 0 & -2 & 2 & 2\end{pmatrix}\\
&\times \begin{pmatrix} D(x,y)\\ D(x,y)\\ D(x,y)\\ D(x,y)\\ D(x,y)\end{pmatrix}.
\end{aligned} \tag{46}$$

The subscript R denotes solutions based on rotational symmetry. Unlike the solutions based on mirror symmetry [Eqs. (19) and (22)], the flat test solutions based on rotational symmetry [Eq. (27)] do not always include the deformation. For example, in the case of the measurement sequence in Fig. 2, the solution for the deformed flat A, which was rotated in the test, does not contain the deformation. It is the same as the solution for the *undeformed* flat, because $D(x,y)$ is purely rotationally variant and the deformation terms cancel out in the solution for flat A [see Eq. (46)]. For this measurement sequence, the difference of the flat-test solutions for flat A based on mirror symmetry and rotational symmetry is the deformation $D(x,y)$.

It is also possible to derive a three-flat solution in closed form, in which the deformation is determined along with flatness errors for the three flats, and which is based on mirror symmetry only. The introduction of a new variable, $D(x,y)$, means that the measurement sequence (BA, BA^R, CA, CB) will not have a solution, and at least one additional measurement must be added to the measurement sequence. One obvious choice is to rotate a second flat, for example flat B, and add the measurement CB^R to the sequence. The equation describing this measurement is

$$W = W_C^x + W_B^R + 2D. \tag{47}$$

It contains two deformation terms for flats B and C. Equation (47) also introduces another variable, W_B^R. This means

that one more measurement must be added to the measurement sequence. For the second additional measurement we return to the measurement W_2. In this measurement, flat A was rotated to remove the rotationally variant component of flat A from the measurement of test flat A against reference flat B. We now rotate this measurement back to the original orientation of flat A. This has the effect of rotating the rotationally variant component of flat B *and* the deformation terms for both flats. These terms can then either be averaged out or be calculated using a difference equation. The resulting wavefront is

$$W = W_B^R + W_A, \tag{48}$$

which does *not* contain a deformation term. The measurement sequence now consists of six measurements: $(BA, BA^R, BA^{-R}, CA, CB, CB^R)$. The notation BA^{-R} is used to indicate the reverse azimuthal averaging that leads to Eq. (48). The three-flat equation for this sequence is

$$\begin{pmatrix} W_1(x,y) \\ W_2(x,y) \\ W_3(x,y) \\ W_4(x,y) \\ W_5(x,y) \\ W_6(x,y) \end{pmatrix} = \begin{pmatrix} 1 & 0 & 1 & 0 & 0 & 0 & 2 \\ 0 & 0 & 1 & 0 & 1 & 0 & 2 \\ 1 & 0 & 0 & 0 & 0 & 1 & 0 \\ 1 & 0 & 0 & 1 & 0 & 0 & 2 \\ 0 & 1 & 0 & 1 & 0 & 0 & 2 \\ 0 & 0 & 0 & 1 & 0 & 1 & 2 \end{pmatrix} \begin{pmatrix} W_A(x,y) \\ W_B(x,y) \\ W_B(-x,y) \\ W_C(-x,y) \\ W_A^R \\ W_B^R \\ D(x,y) \end{pmatrix}. \tag{49}$$

This equation can be solved following a procedure described elsewhere.[18] First, the vector on the right-hand side of Eq. (49) is split into x-even and x-odd components:

$$\begin{pmatrix} W_A(x,y) \\ W_B(x,y) \\ W_B(-x,y) \\ W_C(-x,y) \\ W_A^R \\ W_B^R \\ D(x,y) \end{pmatrix} = \begin{pmatrix} W_A^e(x,y) \\ W_B^e(x,y) \\ W_B^e(x,y) \\ W_C^e(x,y) \\ W_A^R \\ W_B^R \\ D(x,y) \end{pmatrix} + \begin{pmatrix} W_A^o(x,y) \\ W_B^o(x,y) \\ -W_B^o(x,y) \\ -W_C^o(x,y) \\ 0 \\ 0 \\ 0 \end{pmatrix}. \tag{50}$$

The resulting equation for the x-even components is

$$\begin{pmatrix} W_1^e(x,y) \\ W_2^e(x,y) \\ W_3^e(x,y) \\ W_4^e(x,y) \\ W_5^e(x,y) \\ W_6^e(x,y) \end{pmatrix} = \begin{pmatrix} 1 & 1 & 0 & 0 & 0 & 2 \\ 0 & 1 & 0 & 1 & 0 & 2 \\ 1 & 0 & 0 & 0 & 1 & 0 \\ 1 & 0 & 1 & 0 & 0 & 2 \\ 0 & 1 & 1 & 0 & 0 & 2 \\ 0 & 0 & 1 & 0 & 1 & 2 \end{pmatrix} \begin{pmatrix} W_A^e(x,y) \\ W_B^e(x,y) \\ W_C^e(x,y) \\ W_A^R \\ W_B^R \\ D(x,y) \end{pmatrix}. \tag{51}$$

The solution of Eq. (51) for the x-even components is

$$\begin{pmatrix} W_A^e(x,y) \\ W_B^e(x,y) \\ W_C^e(x,y) \\ W_A^R \\ W_B^R \\ D(x,y) \end{pmatrix} = \frac{1}{2} \begin{pmatrix} 0 & 0 & 1 & 1 & 0 & -1 \\ 0 & 0 & 1 & -1 & 2 & -1 \\ -2 & 0 & 1 & 1 & 2 & -1 \\ -2 & 2 & 1 & 1 & 0 & -1 \\ 0 & 0 & 1 & -1 & 0 & 1 \\ 1 & 0 & -1 & 0 & -1 & 1 \end{pmatrix} \times \begin{pmatrix} W_1^e(x,y) \\ W_2^e(x,y) \\ W_3^e(x,y) \\ W_4^e(x,y) \\ W_5^e(x,y) \\ W_6^e(x,y) \end{pmatrix}. \tag{52}$$

For the x-odd wavefront components one obtains the equation

$$\begin{pmatrix} W_1^o(x,y) \\ W_2^o(x,y) \\ W_3^o(x,y) \\ W_4^o(x,y) \\ W_5^o(x,y) \\ W_6^o(x,y) \end{pmatrix} = \begin{pmatrix} 1 & -1 & 0 \\ 0 & -1 & 0 \\ 1 & 0 & 0 \\ 1 & 0 & -1 \\ 0 & 1 & -1 \\ 0 & 0 & -1 \end{pmatrix} \begin{pmatrix} W_A^o(x,y) \\ W_B^o(x,y) \\ W_C^o(x,y) \end{pmatrix}, \tag{53}$$

which can be solved using the pseudoinverse of the coefficient matrix in Eq. (53):

$$\begin{pmatrix} W_A^o(x,y) \\ W_B^o(x,y) \\ W_C^o(x,y) \end{pmatrix} = \frac{1}{4} \begin{pmatrix} 1 & -1 & 2 & 1 & 0 & -1 \\ 1 & -2 & 1 & 0 & 1 & -1 \\ 0 & -1 & 1 & -1 & -1 & -2 \end{pmatrix} \begin{pmatrix} W_1^o(x,y) \\ W_2^o(x,y) \\ W_3^o(x,y) \\ W_4^o(x,y) \\ W_5^o(x,y) \\ W_6^o(x,y) \end{pmatrix}. \tag{54}$$

The solutions for the x-even and x-odd components can now be combined into a single equation for the wavefront flatness errors of the three *undeformed* flats and the mounting-induced deformation in terms of x-even and x-odd components of the measurements $W_1 \ldots W_6$:

$$\begin{pmatrix} W_A(x,y) \\ W_B(x,y) \\ W_C(x,y) \\ D(x,y) \end{pmatrix} = \frac{1}{4}\begin{pmatrix} 0 & 2 & 2 & 0 & -2 & 1 & -1 & 2 & 1 & 0 & -1 \\ 0 & 2 & -2 & 4 & -2 & -1 & -2 & 1 & 0 & 1 & -1 \\ -4 & 2 & 2 & 4 & -2 & 0 & -1 & 1 & -1 & -1 & -2 \\ 2 & -2 & 0 & -2 & 2 & 0 & 0 & 0 & 0 & 0 & 0 \end{pmatrix} \begin{pmatrix} W_1^e(x,y) \\ W_3^e(x,y) \\ W_4^e(x,y) \\ W_5^e(x,y) \\ W_6^e(x,y) \\ W_1^o(x,y) \\ W_2^o(x,y) \\ W_3^o(x,y) \\ W_4^o(x,y) \\ W_5^o(x,y) \\ W_6^o(x,y) \end{pmatrix}. \tag{55}$$

4 Numerical Simulations

We simulated the three-flat tests described in Secs. 2 and 3 to illustrate the effect of mounting-induced distortions on flat test solutions. In Fig. 3 the simulated wavefront flatness errors for three flats are shown, which were generated using Zernike polynomials. With these flatness errors, the measurement sequence (BA, BA^R, CA, CB) of Fig. 2 was simulated. Then, the flat-test solutions based on rotational symmetry and mirror symmetry and described in Sec. 2 were calculated. For both symmetries, the rotationally invariant component of flat A was calculated with n-position averaging and rotational differencing using three rotation angles of 2.9, 13, and 57 deg for flat A. Figure 4 shows the test results for flat A in the absence of noise and measurement errors. The first column of maps in Fig. 4 are the solutions for flat A, which were calculated with Eq. (19). The superscript x is used throughout the paper to identify solutions based on mirror symmetry. In the two solutions with subscript np, n-position averaging was used to calculate the rotationally variant component Ω_A of flat A; for the solution with subscript rd, the difference equation (33) was solved. The top row contains solutions that were calculated with 21-position averaging. The rightmost two columns of Fig. 4 show the difference between the solutions and the known flatness error in Fig. 3. The solutions using 21-position averaging are indistinguishable from those calculated with the rotational differencing method in the bottom row of Fig. 4.

Figure 5 shows the effect of mounting-induced deformations on the flat-test solutions. We assumed that all three flats are subject to the deformation shown in the bottom right corner of Fig. 5. The deformation was obtained by calculating an x-even function—again using Zernike polynomials—which may reasonably be caused by supporting the flat at two points and clamping it at the top. The resulting flat test solutions based on mirror symmetry and rotational symmetry for flat A are shown in Fig. 5. The second column contains solutions based on rotational symmetry, which are identical to the undeformed flatness errors [see Eq. (46)]. This is evident in the last column, which compares the solutions based on rotational symmetry with the true form of flat A shown in Fig. 3. In the first column are the corresponding solutions based on mirror symmetry. These solutions differ from the true form of the flat by the deformation [see Eq. (45)].

Figure 6 illustrates the flat test solution in Eq. (55). The measurement sequence (BA, BA^R, BA^{-R}, CA, CB, CB^R) was simulated using the flatness errors shown in Fig. 3 and the deformation shown in Fig. 5. The undeformed flat solutions, which were calculated with Eq. (55), are shown in the top row of Fig. 6 along with the solution for the mounting-induced deformation.

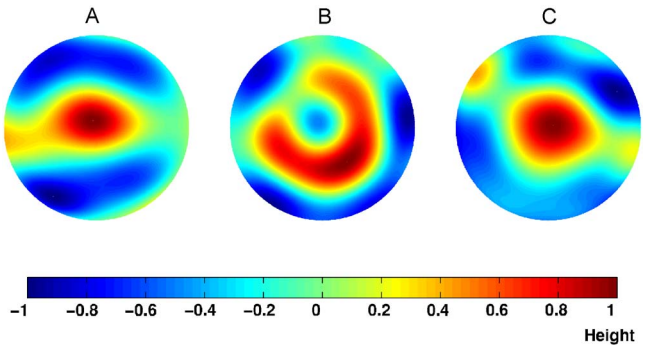

Fig. 3 Simulated flatness errors of three flats A, B, and C.

5 Measurements

We now demonstrate the three-flat tests of Sec. 2 with the calibration of reference flats for XCALIBIR at the National Institute of Standards and Technology (NIST). XCALIBIR is a multiconfiguration interferometer that can be set up as a Fizeau interferometer with a collimated test beam of 300-mm diameter. A solid model of the interferometer in this configuration is shown in Fig. 7. The interferometer is built on a granite table to minimize seismic vibrations. Source and imaging optics are set up on an elevated optical breadboard to create sufficient clearance for the testing of larger optics. Light from a tunable, single-frequency diode laser is delivered to the interferometer with optical fibers. A wavemeter references the laser wavelength to the known wavelength of either a helium-neon laser or a spectral line

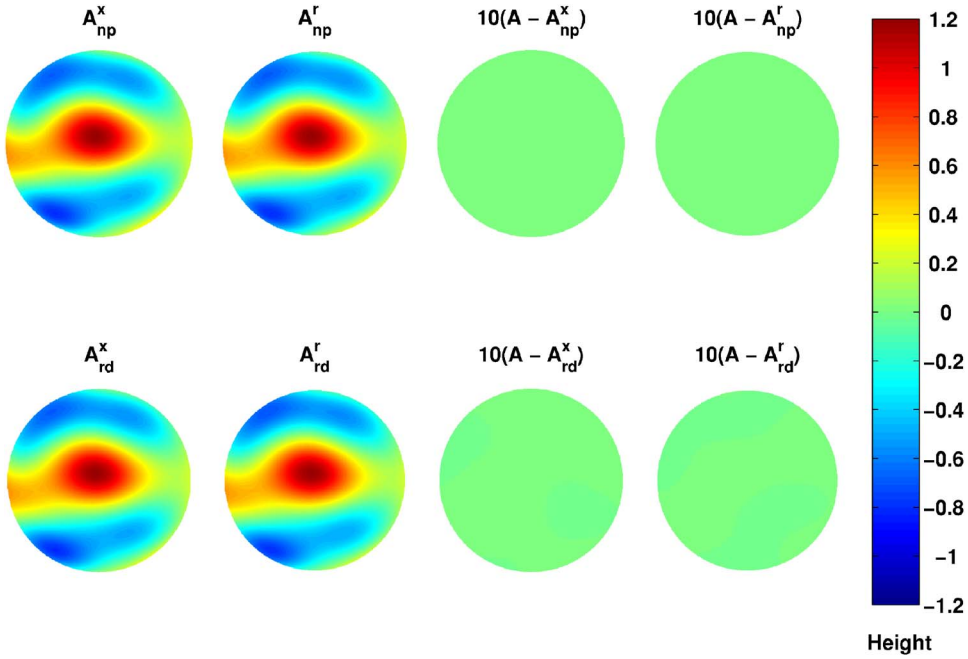

Fig. 4 Three-flat test solutions for flat *A* without mounting-induced errors using 21-position averaging (top row) and rotational differencing (bottom row). The superscript *x* indicates a solution based on mirror symmetry; a superscript *r* one based on rotational symmetry. A subscript *np* indicates that *n*-position averaging was used; a subscript *rd*, that rotation differencing was used.

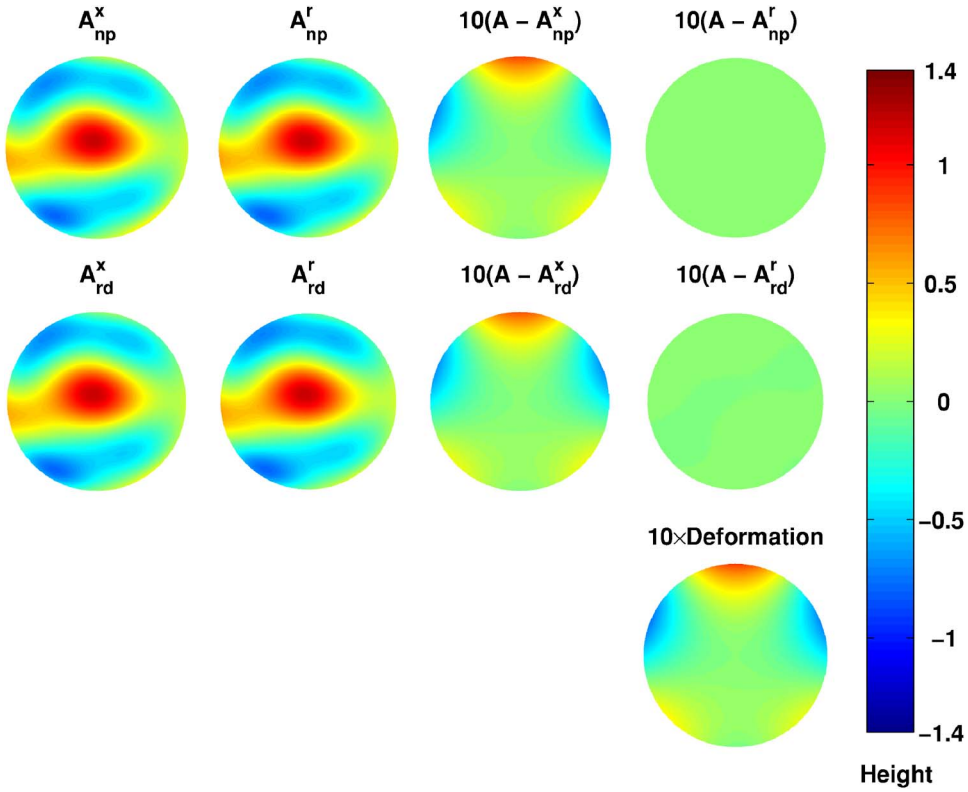

Fig. 5 Numerical simulation of three-flat tests in the presence of errors introduced by the mounting of the flats. The three-flat solutions for flat *A* based on mirror symmetry [Eq. (19)] and rotational symmetry [Eq. (27)] are shown. The assumed mounting-induced error is shown in the bottom right corner.

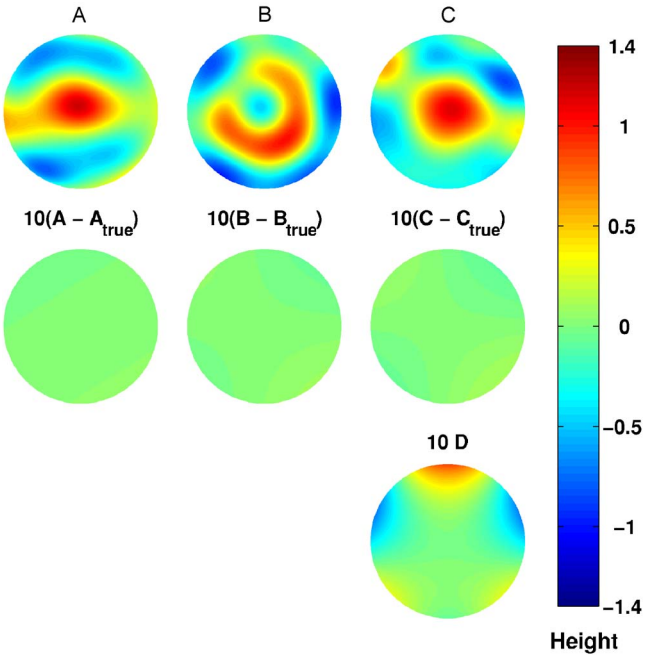

Fig. 6 Numerical simulation of three-flat test solution in Eq. (55). The six measurements of the sequence (BA, BA^R, BA^{-R}, CA, CB, CB^R) are solved for the flatness errors of the undeformed flats and the deformation D. The solutions are compared with the known flatness errors in Fig. 3 in the second row.

of a neon glow discharge, and thus establishes traceability to the SI unit of length. An off-axis parabolic mirror collimates the central portion of the light cone, which is emitted by the optical fiber and creates a collimated beam parallel to the top surface of the granite table. A beam expander, consisting of an f/4 diverger lens (DL in Fig. 7) and an f/4 collimator lens (CL), creates a collimated test beam with just above 300-mm diameter. XCALIBIR is equipped with a set of three fused-silica flats with a diameter of 325 mm and a thickness of 64 mm. The test flat (TF) is installed on a mount that can be piezomechanically phase-shifted. The return beams from the reference flat (RF) and test flat (TF) are directed to the imaging arm of the interferometer by a

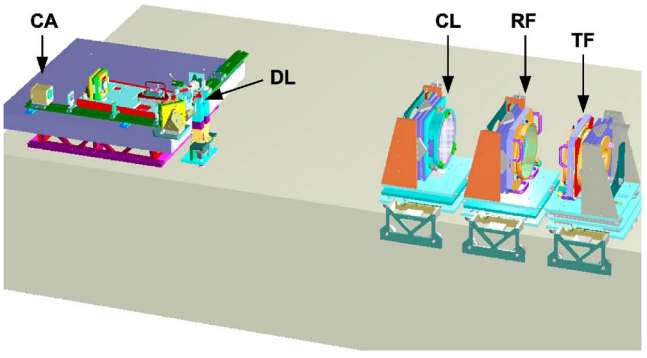

Fig. 7 XCALIBIR interferometer in Fizeau configuration with collimated test beam and 300-mm aperture. The main components of the interferometer, from left to right, are: breadboard with light source, imaging optics, camera (CA), diverger lens (DL), collimator lens (CL), reference flat (RF), and test flat (TF).

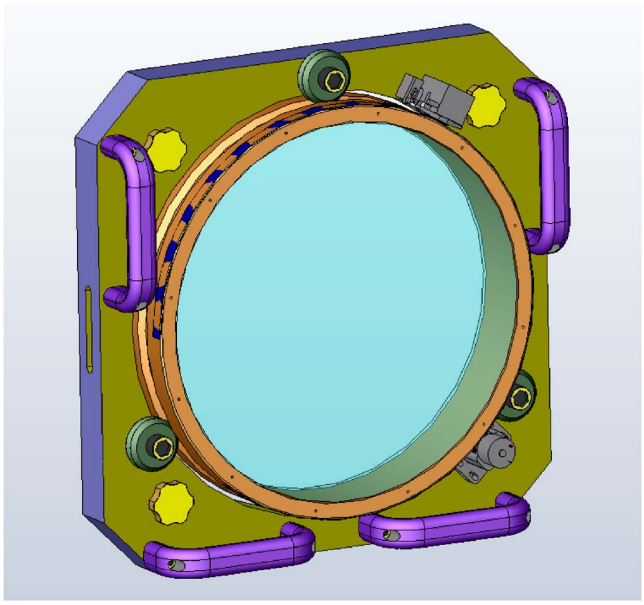

Fig. 8 Solid model of a rotatable flat mount for a 325-mm flat for the XCALIBIR interferometer at NIST. A drive wheel on a small electrical motor is used to rotate the flat. It can be seen in the bottom right of the picture.

beamsplitter on the optical breadboard. The camera of XCALIBIR has 1024×1024 pixels which corresponds to a spatial resolution of about 0.3 mm for the 300-mm aperture when the image detector is nearly filled.

A critical aspect of interferometric flatness metrology is the mounting of the test and reference flats. A mount should not distort the flat in an unpredictable way, and the flat must not deform when it is unmounted and then remounted or, as is necessary for a three-flat test, when it is rotated. This may be difficult to accomplish with large flats. For the set of flats for the XCALIBIR interferometer, we developed the mounts shown in Fig. 8. The flats are bonded to an aluminum collar with a silicone elastomer adhesive. The adhesive was injected through 12 holes in the hoop into the 1-mm-wide gap between flat and metal collar to form circular pads, which are approximately 30 mm in diameter. The metal collar has a groove for three V bearings, which hold the flat. The flats can be rotated using small electric motors like the one that is visible on the bottom right of Fig. 8 on the frame that holds the bearings. When a measurement for a three-flat test is made, the flats must first be centered in a reproducible fashion and rotated to a known orientation. This is achieved with the aid of six fiducial markings located on a circle with 300-mm diameter, which has its center on the axis of rotation. Each of the three flats has the same set of six fiducial marks. The fiducials can also be used to rotate one flat by 60 deg relative to another while maintaining a common center. This was used to implement the six-position tests described below.

Prior to calibration measurements, it is necessary to characterize the lateral distortion of the interferometer's imaging system. For the flat test configuration of XCALIBIR, the distortion was characterized by placing a mask with a square grid of holes in front of the test flat. The mask is shown in Fig. 9. The holes have a 2-mm diameter and a

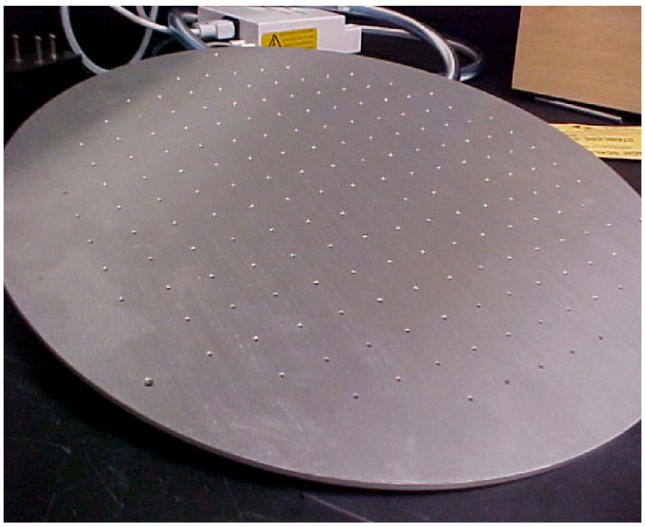

Fig. 9 Mask with a 20-mm square grid of holes of 2-mm diameter, which is imaged onto the detector.

20-mm spacing in the horizontal and vertical directions. This square pattern of holes was imaged on the detector by the interferometer, and the distances of the hole images on the detector in the vertical and horizontal direction were determined. Each hole creates an image, which is a few pixels in diameter. The intensity centroid of these pixels was used as an estimate of the hole image position. The resulting distribution of horizontal and vertical distances, in detector pixels, is shown in Fig. 10. The mean distance between hole images, μ, is 60.06 pixels, which corresponds to a spatial resolution of the interferometer of 333 μm/pixel. The standard deviation of the distribution, σ, is 0.27 pixels, which is well below one pixel. The distribution is slightly skewed towards shorter distances with skewness $\gamma=-0.3$, which is likely caused by a slight shortening of the hole image distances at the edge of the field of view. The magnitude of the distortion is so low that it could be neglected for the measurements described in this paper.

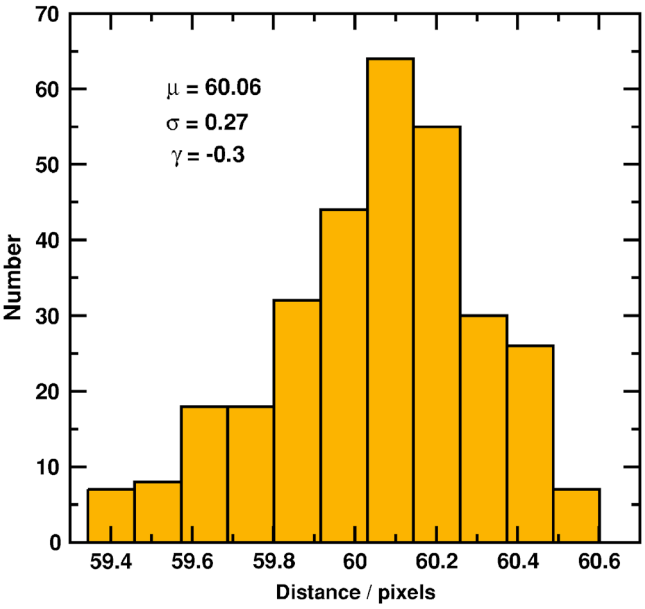

Fig. 10 Histogram of numbers of vertical and horizontal distances between hole images on the detector, in pixels. The bin width is 0.14 pixels.

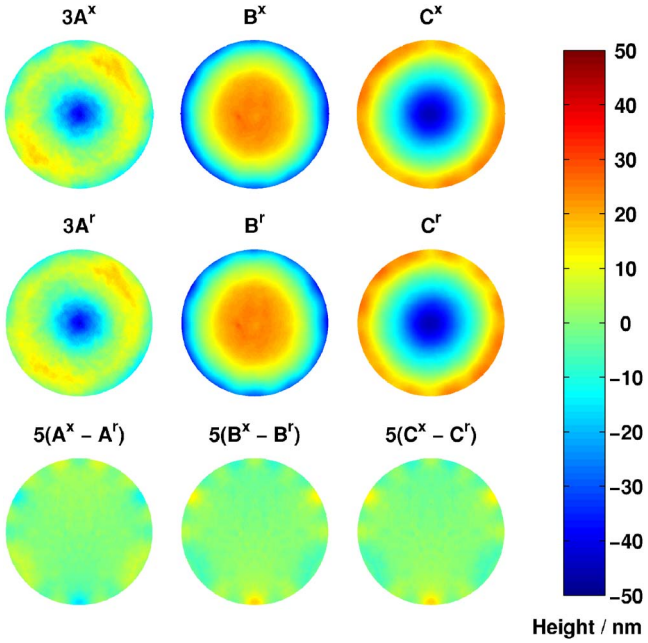

Fig. 11 Surface flatness errors of three 325-mm flats. The clear aperture of 300 mm is shown. The rotationally variant component of flat A was measured with a six-position averaging test. Test solutions based on mirror symmetry (A^x, B^x, C^x) and rotational symmetry (A^r, B^r, C^r) are shown. The bottom row shows the difference between the two types of solution.

Several three-flat tests of NIST's 325-mm flats were made with the XCALIBIR interferometer to compare with the tests described in Sec. 2. Results of a three-flat test, with six-position averaging of flat A, are shown in Fig. 11. Solutions based on mirror symmetry and rotational symmetry are shown, along with their differences. Figure 12 compares the solutions for flat A in more detail. The solutions shown are based on mirror (A^x) and rotation (A^r) symmetries [Eqs. (19) and (27)]. The subscript np indicates that six-position averaging was used to determine Ω_A, and the subscript rd indicates that rotational differencing was used. In the latter case, flat A was rotated by 3.14, 11.91, and 40.93 deg. The first column of images in Fig. 12 shows solutions for NIST flat A based on mirror symmetry; the second column shows the corresponding solutions based on rotational symmetry. The difference of these solutions, which is the mounting-induced deformation of NIST flat A, is shown in the third column. In the map at the top of the third column, the flatness error of flat A was measured using a six-position average. The residual error with 12-fold symmetry near the edge of the flat is caused by the 12 mounting pads of the flat. These cause a flatness error with 12-fold symmetry, which is not averaged out by the six-position average. This error is not present in the map at the bottom of the third column because it was calculated using rotational differencing. The mounting-induced deformation is largest at the points where the aluminum collar around

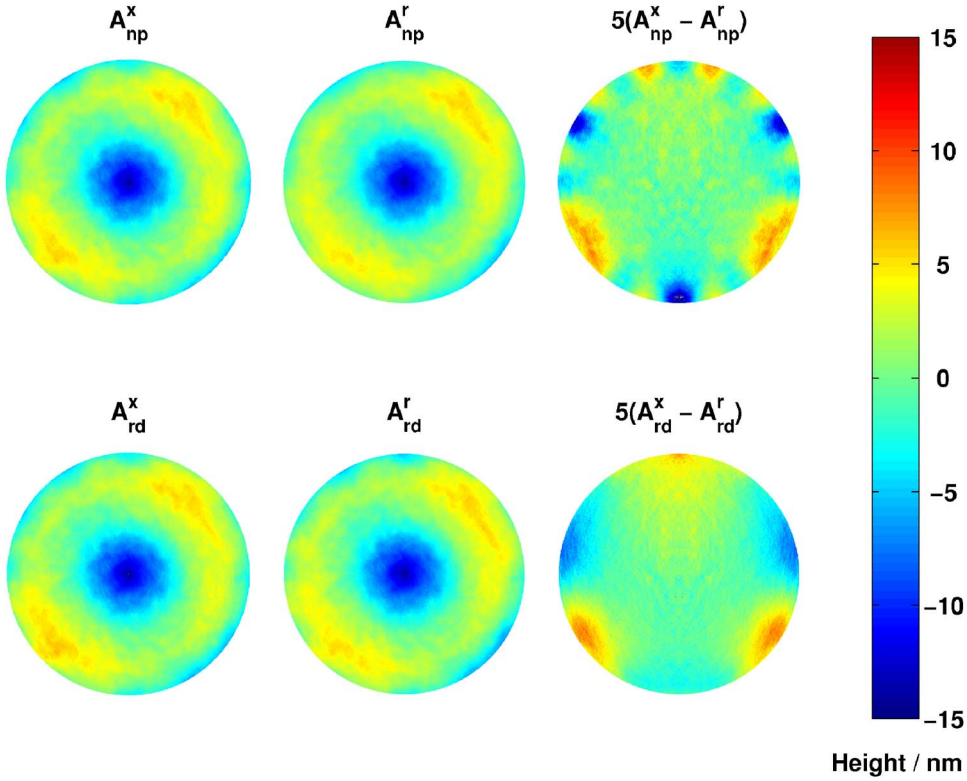

Fig. 12 Surface flatness error of 325-mm flat *A*. The clear aperture of 300 mm is shown. The solutions with subscript *rd* used the rotational differencing method with Fourier representation of circular profiles[12] to determine Ω_A (see Sec. 2.3). The third column shows the mounting-induced deformation of NIST flat *A*, which amounts to about 5 nm peak to valley.

the flat rests on the two V bearings, and an increase in the deformation is also observed near the V bearing at the top of the metal collar (see Fig. 8). The magnitude of the mounting-induced deformation is approximately 5 nm peak to valley.

6 Repeatability

Few analyses of measurement repeatability or uncertainty of three-flat tests have been described in the literature.[19,20] We show that the simple form of the three-flat test solutions (19) and (27) facilitates the calculation of uncertainties for the flat test solutions. The four measurements $W_1(x,y),\ldots,W_4(x,y)$ of the three-flat test sequence (BA, BA^R, CA, CB) in Fig. 2 have uncertainties $\delta W_1(x,y),\ldots,\delta W_4(x,y)$, which, like the measurements $W_i(x,y)$, are functions of two variables and describe the measurement uncertainty at each point, or pixel, of the measurements. The three-flat test solutions (13), (27), and (19), are linear equations of the form

$$W_k(x,y) = \sum_m C_{km} S_m(x,y), \tag{56}$$

where S_m are the symmetry components of the wavefront measurements, C_{km} constitute a matrix, and W_k are the flat test solutions. When uncorrelated pixels are assumed, formulas for the propagation of uncertainty[21,22] can be applied to Eq. (56) to calculate the variances of the test solutions from the variances of the symmetry components of the wavefront measurements:

$$[\delta W_k(x,y)]^2 = \sum_m C_{km}^2 [\delta S_m(x,y)]^2. \tag{57}$$

As an example, we derive approximate expressions for the variances of the three-flat test solutions based on mirror symmetry, which directly link the variances of the solutions to the variances of the wavefront measurements. First, the uncertainties of the symmetry components of the measurements must be determined. The measurements $W_i(x,y)$ are separated into x-even and x-odd components $W^e(x,y)$ and $W^o(x,y)$ according to Eq. (16). It is assumed that the uncertainties at each point of $W_i(x,y)$ are uncorrelated and that $\delta W_i \approx \delta W_i^x$. The uncertainties of the x-even and x-odd components can then be calculated:

$$\delta W_i^e(x,y) = \delta W_i^o(x,y) = \frac{1}{\sqrt{2}} \delta W_i(x,y), \quad i = 1,\ldots,4. \tag{58}$$

When the error propagation formula is applied to Eq. (19) to calculate the variances δW_A^2, δW_B^2, and δW_C^2 for the three-flat test solutions, the following equation results:

$$\begin{pmatrix} [\delta W_A(x,y)]^2 \\ [\delta W_B(x,y)]^2 \\ [\delta W_C(x,y)]^2 \end{pmatrix} = \frac{1}{8}\begin{pmatrix} 5 & 4 & 1 & 1 \\ 1 & 4 & 1 & 1 \\ 5 & 5 & 5 & 4 \end{pmatrix}\begin{pmatrix} [\delta W_1(x,y)]^2 \\ [\delta W_2(x,y)]^2 \\ [\delta W_3(x,y)]^2 \\ [\delta W_4(x,y)]^2 \end{pmatrix}, \quad (59)$$

which relates the variances of the test solutions to the variances of the initial measurements and allows the uncertainties of the flat test solutions to be calculated from the measurement uncertainties.

Different methods for solving the three-flat problem lead to different uncertainties for the flat test solutions. This can be seen when wavefront variances are calculated for the alternative test solution in Eq. (22), which yields the following result for the variances of the test solutions:

$$\begin{pmatrix} [\delta W_A(x,y)]^2 \\ [\delta W_B(x,y)]^2 \\ [\delta W_C(x,y)]^2 \end{pmatrix} = \frac{1}{72}\begin{pmatrix} 25 & 36 & 13 & 13 \\ 9 & 36 & 9 & 9 \\ 13 & 36 & 13 & 25 \end{pmatrix}\begin{pmatrix} [\delta W_1(x,y)]^2 \\ [\delta W_2(x,y)]^2 \\ [\delta W_3(x,y)]^2 \\ [\delta W_4(x,y)]^2 \end{pmatrix}. \quad (60)$$

For identical measurement variances $\delta W_1, \ldots, \delta W_4$, the alternative solutions in Eq. (22) have slightly lower variances than the solution Eq. (19). In both cases, the solutions for flat B have the lowest variance. This is not generally the case, and a test solution based on mirror symmetry is known for which flat A has the lowest variance.[18] Overall, the lowest variances for test solutions are achieved in tests in which all three flats are rotated.[18]

We illustrate Eq. (59) by calculating the uncertainty for the flat test solutions shown in Fig. 11. The measurements $W_1, \ldots, W_4$ in Fig. 2 were each repeated 20 times. The measurements of W_2 were made with six-position averaging. At each of the pixels of the measurements, the standard deviations $\delta W_i(x,y)$ of the combined wavefront measurements were calculated. The resulting maps are shown in the first two rows of Fig. 13. The wavefront W_2 was calculated using both six-position averaging [Eq. (41)] and rotational differencing [Eq. (33)]. At the center, all maps have a small area with increased uncertainty, which is caused by a small hot spot of the interferometer. The other areas with increased uncertainty are either small circular shapes that are caused by screw heads, which have a higher reflectivity than the surrounding black anodized metal parts, or by pieces of adhesive tape on the mount. The wavy variations, especially in δW_1, can be traced to vibration of the mounts during the measurements. The measurements also show that the assumption $\delta W_i = \delta W_i^x$, which was made in the derivation of Eq. (59), is justified. The standard deviations in $\delta W_2(np)$ are lower than in the other maps because of the sixfold averaging of the dominant rotation-invariant component of the rotated flat A. Using Eq.(59), the standard deviation maps for the three-flat solution wavefronts were calculated. The third row of Fig. 13 shows the uncertainty for the three-flat test solutions that were obtained with six-position averaging. The bottom row shows the uncertainty of the same test solutions obtained with rotational differencing using the three rotation angles 3.14, 11.91, and 40.93 deg.

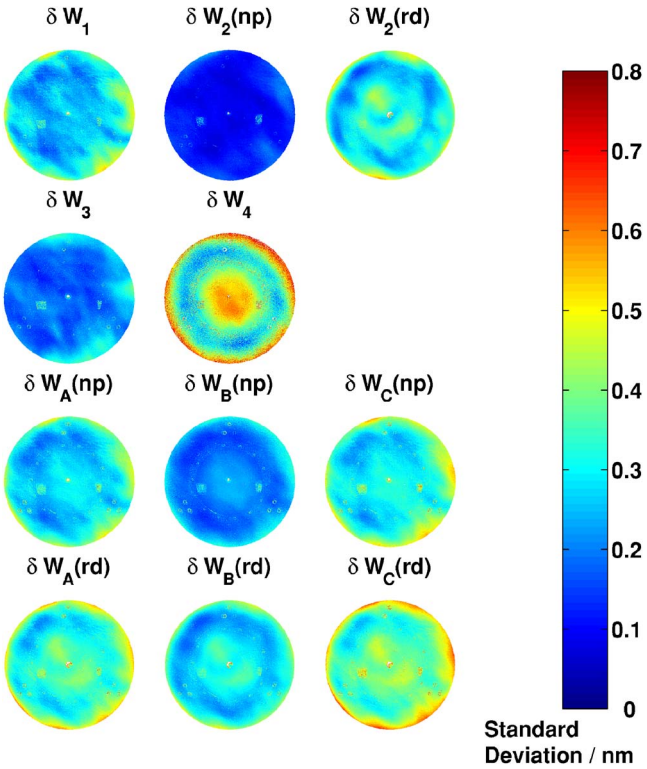

Fig. 13 Standard deviation for each pixel of 20 wavefront flatness measurements $W_1, \ldots, W_4$ and standard deviation maps of three-flat test solution wavefronts based on mirror symmetry for NIST flats A, B, and C using six-position averaging (third row) and rotational differencing (bottom row). Equation (59) was used to calculate the standard deviation maps for the test solutions.

It is often desirable to quantify the measurement uncertainty with a single number instead of an uncertainty map. Table 1 lists often used metrics for the data variation in a map, the mean of all pixels, the root mean square (rms),

Table 1 Mean, rms, and peak (with 0.1% of extreme values removed) of the standard deviation maps for the wavefront flatness error of NIST flats A, B, and C shown in Fig. 13. The standard deviations for the flat surfaces are calculated by dividing all numbers by two [Eq. (2)].

	Six-position averaging			Rotational differencing		
Map	Mean (nm)	Rms (nm)	Peak (99.9%) (nm)	Mean (nm)	Rms (nm)	Peak (99.9%) (nm)
δW_1	0.28	0.30	0.53	0.28	0.30	0.53
δW_2	0.11	0.12	0.27	0.31	0.32	0.57
δW_3	0.20	0.22	0.43	0.20	0.22	0.43
δW_4	0.42	0.45	1.11	0.42	0.45	1.11
δW_A	0.29	0.31	0.55	0.35	0.37	0.66
δW_B	0.21	0.22	0.45	0.29	0.30	0.59
δW_C	0.33	0.30	0.60	0.40	0.41	0.72

and the peak, for the standard deviation maps in Fig. 13. In the calculation of the peak numbers, 0.1% of the pixels with the largest uncertainty were considered outliers and were not included.

7 Conclusion

In any measurement it is desirable to be limited only by measurement repeatability. We have shown that in three-flat tests of large flats, deformations of the flats due to the support mechanism can give rise to measurement errors, which can be much larger than the repeatability. For example, in the case of our flats at NIST with 325-mm diameter, we found that the mounting-induced deformation of the flats is about 5 nm (peak to valley), which is approximately 10 times larger than the expanded ($k=2$) repeatability of our measurements. Correct treatment of mounting-induced deformations is necessary for three-flat tests with uncertainties at the nanometer level, especially for large flats. We show that the effect of deformations can be determined in the flat test when the mechanical support of the flats imparts a purely x-even deformation. For the practitioner of three-flat testing it is useful to know that flat test solutions based on mirror symmetry[18] always contain the deformation, whereas solutions based on rotational symmetry may not. The difference between the two types of solutions can be used to determine the deformation as long as the deformations of the flats are identical.

Acknowledgments

We are deeply grateful to Dr. Robert S. Polvani for his unwavering support of the Advanced Optics Metrology effort at NIST. We also thank him, Dr. Mahn-Hee Hahn, and Jarred Heigel, both at NIST, for their contribution to the design of flat mounts. We thank Dr. Michael Küchel, at Zygo Corporation, for brief but helpful comments on our measurements, and Dr. Chris J. Evans, also at Zygo Corporation, for reading the manuscript and for insightful comments.

References

1. J. W. Strutt (Lord Rayleigh), "Interference bands and their applications," *Nature* **48**, 212–214 (1893).
2. R. Bünnagel, "Untersuchungen über die Eignung eines Flüssigkeitsspiegels als Ebenheitsnormal," *Z. Angew. Phys.* **8**, 342–350 (1956).
3. I. Powell and E. Goulet, "Absolute figure measurements with a liquid-flat reference," *Appl. Opt.* **37**, 2579–2586 (1998).
4. M. V. Mantravadi, "Newton, Fizeau, and Haidinger interferometers," in *Optical Shop Testing*, 2nd ed., D. Malacara, Ed., pp. 1–49, Wiley, New York (1992).
5. R. E. Parks, L. Shao, and C. J. Evans, "Pixel-based absolute topography test for three flats," *Appl. Opt.* **37**, 5951–5956 (1998).
6. C. Ai and J. C. Wyant, "Absolute testing of flats by using even and odd functions," *Appl. Opt.* **32**, 4698–4705 (1993).
7. M. F. Küchel, "A new approach to solve the three flat problem," *Optik (Jena)* **112**, 381–391 (2001).
8. C. J. Evans and R. N. Kestner, "Test optics error removal," *Appl. Opt.* **35**, 1015–1021 (1996).
9. R. E. Parks, "Removal of test optics errors," in Advances in Optical Metrology I, N. Balasubramanian and J. C. Wyant, Eds., *Proc. SPIE* **153**, 56–63 (1978).
10. D. Malacara and S. L. DeVore, "Interferogram evaluation and wavefront fitting," in *Optical Shop Testing*, 2nd ed., D. Malacara, Ed., pp. 455–499, Wiley, New York (1992).
11. S. C. Verrall and R. Kakarala, "Disk-harmonic coefficients for invariant pattern recognition," *J. Opt. Soc. Am. A* **15**, 389–401 (1998).
12. K. R. Freischlad, "Absolute interferometric testing based on reconstruction of rotational shear," *Appl. Opt.* **40**, 1637–1648 (2001).
13. R. P. Bourgeois, J. Magner, and H. P. Stahl, "Results of the calibration of interferometer transmission flats for the LIGO pathfinder optics," in Optical Manufacturing and Testing II, H. P. Stahl, Ed., *Proc. SPIE* **3134**, 86–94 (1997).
14. B. S. Fritz, "Absolute calibration of an optical flat," *Opt. Eng.* **23**, 379–383 (1984).
15. D. J. Whitehouse, "Some theoretical aspects of error separation techniques in surface metrology," *J. Phys. E* **9**, 531–536 (1976).
16. W. T. Estler, C. J. Evans, and L. Z. Shao, "Uncertainty estimation for multiposition form error metrology," *Precis. Eng.* **21**, 72–82 (1997).
17. R. E. Parks, C. J. Evans, P. J. Sullivan, L.-Z. Shao, and B. Loucks, "Measurements of the LIGO pathfinder optics," in Optical Manufacturing and Testing II, H. P. Stahl, Ed., *Proc. SPIE* **3134**, 95–111 (1997).
18. U. Griesmann, "Three-flat test solutions based on simple mirror symmetry," *Appl. Opt.* **45**, 5856–5865 (2006).
19. V. Greco, R. Tronconi, C. D. Veccio, M. Trivi, and G. Molesini, "Absolute measurement of planarity with Fritz's method: uncertainty evaluation," *Appl. Opt.* **38**, 2018–2027 (1999).
20. G. Schulz and J. Grzanna, "Absolute flatness testing by the rotation method with optimal measuring-error compensation," *Appl. Opt.* **31**, 3767–3780 (1990).
21. H. H. Ku, "Notes on the use of propagation of error formulas," *J. Res. Natl. Bur. Stand., Sect. C* **70C**, 263–273 (1966).
22. B. N. Taylor and C. E. Kuyatt, "Guidelines for evaluating and expressing the uncertainty of NIST measurement results; NIST Technical Note 1297," U.S. Government Printing Office, Washington (1994).

Ulf Griesmann is a physicist with the National Institute of Standards and Technology. He received his DrRerNat degree from the University in Bonn, Germany, in 1992. He worked as a postdoc on atomic spectroscopy with short-wavelength lasers at Imperial College London, United Kingdom. After coming to NIST in 1994, he worked on precision spectrometry and properties of optical materials. His current research interests include optical phase-measuring interferometry, precision form metrology, methods for absolute metrology, and metrology for free-form surfaces.

Quandou Wang is an optical engineer with the National Institute of Standards and Technology. He received his PhD from the Changchun Institute of Optics, Fine Mechanics and Physics (CIOMP), Chinese Academy of Sciences, in 2001. He was with CIOMP from 1992 to 2001. He was with Optical Sciences Center, University of Arizona, from 2001 to 2002, working on computer-controlled optical fabrication and testing of aspherical surfaces. His research interests include optical testing and precision metrology, optomechanics, optical instrument design, and fabrication of aspheric surfaces.

Johannes Soons leads the Manufacturing Process Metrology Group at the National Institute of Standards and Technology. He holds a PhD from the Eindhoven University of Technology in the Netherlands. His professional interests include precision machining and optical testing.